

Automated Delineation of Dry and Melt Snow Zones in Antarctica Using Active and Passive Microwave Observations From Space

Hongxing Liu, *Member, IEEE*, Lei Wang, and Kenneth C. Jezek, *Associate Member, IEEE*

Abstract—This paper presents the algorithms and analysis results for delineating snow zones using active and passive microwave satellite remote sensing data. With a high-resolution Radarsat synthetic aperture radar (SAR) image mosaic, dry snow zones, percolation zones, wet snow zones, and blue ice patches for the Antarctic continent have been successfully delineated. A competing region growing and merging algorithm is used to initially segment the SAR images into a series of homogeneous regions. Based on the backscatter characteristics and texture property, these image regions are classified into different snow zones. The higher level of knowledge about the areal size of and adjacency relationship between snow zones is incorporated into the algorithms to correct classification errors caused by the SAR image noise and relief-induced radiometric distortions. Mathematical morphology operations and a line-tracing algorithm are designed to extract a vector line representation of snow-zone boundaries. With the daily passive microwave Special Sensor Microwave/Imager (SSM/I) data, dry and melt snow zones were derived using a multiscale wavelet-transform-based method. The analysis results respectively derived from Radarsat SAR and SSM/I data were compared and correlated. The complementary nature and comparative advantages of frequently repeated passive microwave data and spatially detailed radar imagery for detecting and characterizing snow zones were demonstrated.

Index Terms—Antarctica, passive microwave, snow zones, synthetic aperture radar (SAR).

I. INTRODUCTION

THE METAMORPHOSIS of snow and firn is strongly controlled by the amount of snow accumulation, annual surface-temperature variation, and the intensity of summer melt, which vary spatially with geographical location, surface elevation, and regional climate. Depending on the interplay between these factors, distinct snow morphologies arise, which can be used to spatially classify the snow pack into snow zones [1], [2]. Based on field observations from snow pits and cores in the Greenland ice sheet, Benson [1] developed a general snow-zone model. In this model, the surface area of an ice sheet or a glacier is subdivided into four distinct snow zones (facies): the superimposed (bare) ice zone, the wet (soaked) snow zone, the

percolation zone, and the dry snow zone. Long-term variations in areal extent of different snow zones contribute to changes in the Earth's radiation budget, and hence to climate changes [3]. The balance between accumulation and melt in different snow zones also affects the runoff and discharge of stream systems fed by snow and glacier melt water. Moreover, snow pack is extremely sensitive to atmospheric temperature. Spatial extent and geographical position of different snow zones indicate regional climate condition [4]–[6].

Since the publication of Benson's [1] classification scheme in the early 1960s, many investigators have employed satellite remote sensing data to detect these snow zones. Passive microwave data acquired by the Scanning Multichannel Microwave Radiometer (SMMR) onboard the Nimbus-7 satellite and the Special Sensor Microwave/Imager (SSM/I) from the Defense Meteorological Satellite Program (DMSP) have been widely used to detect snow-melt occurrences and to map melt snow zones versus dry snow zones on a large geographical scale [7], [8]. Active microwave radar images are demonstrably effective for a detailed snow-zone recognition and delineation [5], [6], and [9]–[11]. Due to their complementary nature in spatial and temporal resolution, the combination of active and passive microwave data may improve snow-zone detection and interpretation. However, appropriate algorithms are needed to conflate and assimilate the data sets. Up to date, most previous investigators used visual interpretations and manual tracing methods to delineate the snow zones. In addition, earlier research efforts to map snow zones concentrated on the Greenland ice sheet [1], [9]–[11] and some Alpine glaciers [4], [5]. Little research in this aspect has been reported for the much larger Antarctic ice sheet, with the exception of the recent work of Rau and Braun [6] on the Antarctic Peninsula.

In this paper, we present numerical algorithms and analysis results for delineating snow zones in Antarctica with active microwave Radarsat synthetic aperture radar (SAR) imagery and passive microwave SSM/I data. Based on radar-backscatter characteristics of different snow zones, we developed a numerical method to derive snow zones from SAR imagery. With high-resolution Radarsat SAR imagery acquired in 1997, we delineated dry snow zones, percolation zones, wet snow zones, and blue ice patches over the entire Antarctic ice sheet and surrounding ice shelves. Using the passive microwave data, we also derived the snow-melt onset date, melt end date, and melt duration for the period 1991–1997 with a multiscale wavelet-transform-based method [12]. We compared and interpreted the analysis results derived, respectively, from the Radarsat SAR data and the SSM/I data.

Manuscript received March 24, 2005; revised January 18, 2006. This work was supported in part by the National Aeronautics and Space Administration under Grant NAG5-10112 and in part by the National Science Foundation under Grant 0126149.

H. Liu and L. Wang are with the Department of Geography, Texas A&M University, College Station, TX 77843 USA (e-mail: liu@geog.tamu.edu; wanglei@geog.tamu.edu).

K. C. Jezek is with the Byrd Polar Research Center, The Ohio State University, Columbus, OH 43210 USA (e-mail: jezek@frosty.mps.ohio-state.edu).

Digital Object Identifier 10.1109/TGRS.2006.872132

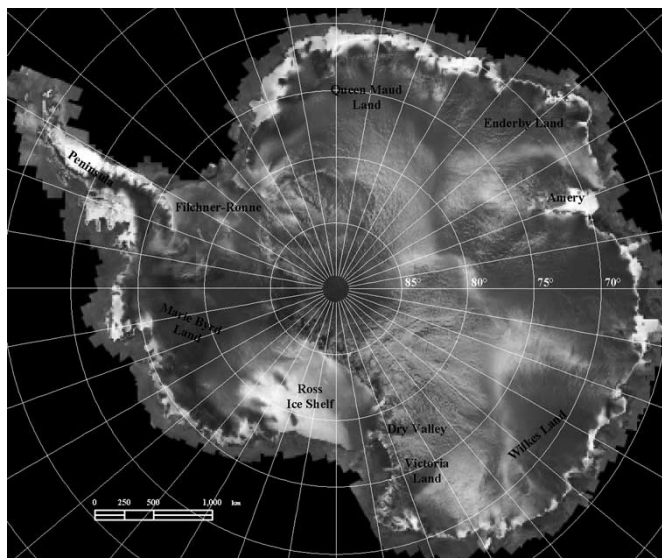


Fig. 1. Orthorectified SAR image mosaic for Antarctica, in which source images were acquired in September and October, 1997 by a Radarsat-1 C-band SAR sensor.

II. DELINEATION OF SNOW ZONES USING RADARSAT SAR IMAGERY

A. Orthorectified Radarsat SAR Image Mosaic for Antarctica

Antarctica is dominated by a vast ice sheet that extends outward on the surrounding ocean in the form of massive ice shelves (Fig. 1). The size of the Antarctic continent approximates the areas of the U.S. and Mexico combined and is 6.4 times as large as Greenland.

We use the Radarsat-1 SAR image mosaic of Antarctica for the snow-zone delineation. The mosaic was compiled from data acquired by a C-band (5.6-cm wavelength) SAR sensor onboard the Canadian Radarsat-1 satellite. The imaging campaign was conducted from September 9 to October 20, 1997 [13]. The coastal regions were imaged mainly using the standard beam 2 with a nominal incidence angle of 24° – 31° at a 25-m resolution. The combination of over 4000 SAR image frames (100 km by 100 km each frame) collected over 30 days provides a high-resolution view of the entire Antarctic continent and offshore ocean.

Through block bundle adjustment, terrain correction, and radiometric balancing operations, a complete seamless orthorectified SAR image mosaic has been produced [13], [14] (Fig. 1). The orthorectified SAR image mosaic is in the polar stereographic projection with reference to the WGS84 ellipsoid. The radiometric balancing operation minimizes the radiometric differences between adjacent image frames and also reduces the radiometric distortions introduced by terrain relief and local incidence-angle variations. The orthorectification process ensures the positional accuracy of the source SAR images, and hence the geographic position and geometric shape of the derived snow-zone boundaries. The absolute geolocation accuracy of the SAR image mosaic is estimated to be approximately 100 m. This precisely geocoded and terrain-corrected image mosaic furnishes a planimetrically accurate radar image base for interpreting and delineating different snow zones at a continental scale.

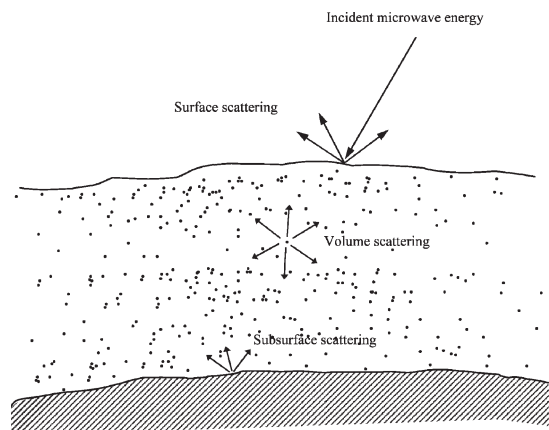


Fig. 2. Components of radar backscattering in the snow pack.

B. Radar-Backscattering Characteristics of Different Snow Zones

A spaceborne SAR sensor is an active microwave imaging system. The radar backscatter received by the SAR sensor is the sum of surface scattering at the air/snow interface, volumetric scattering within the snowpack, and scattering at the snow/bedrock interface (Fig. 2). The bedrock backscatter is negligible in Antarctica due to the great depth of the snow pack.

In different snow zones, snow grain size and density, stratigraphy, surface roughness, and water content of the snow pack are different. These factors affect the surface and volume backscatter strength of the radar signal, and consequently the brightness variation in radar imagery. The contrasts in radar-backscatter strength between different zones permit snow zones to be delineated from SAR image data. The responses of radar signal to snow zones vary from season to season. Previous studies have demonstrated that the winter SAR image acquisitions have much stronger brightness contrasts between adjacent zones than summer acquisitions [5], [6], [11]. The 1997 Radarsat SAR image mosaic of Antarctica was compiled based on the image data acquired during the austral winter season. Therefore, the direct effect of surface melting is minimized, and the radar backscattering is mainly influenced by the grain size, density, stratigraphy, and surface roughness of snow pack.

In this paper, we adopt the terminology and the general snow-zone model in [1] and [2] as the conceptual framework for our snow-zone recognition and delineation effort. In the general snow-zone model, the superimposed ice zone, the wet snow zone, the percolation zone, and the dry snow zone form an ordered sequence from the ice front to the interior of the ice sheet. The combination of the percolation zone, the wet snow zone, and the superimposed ice zone represents the total area affected by surface melting and is referred to as the melt snow zone in this paper (Fig. 3).

In the dry snow zone, melting does not occur even during summers. The prevailing dry-snow metamorphism includes gradual compaction due to its own weight (gravity) and wind action, recrystallization, and depth-hoar development due to internal temperature and moisture gradients. Owing to the absence of melt events, the upper part of the dry snow zone has a low snow density, uniform crystals of small grain size, and a moderately layered snow pack without melt-related ice layers. The interaction between the radar signal and the

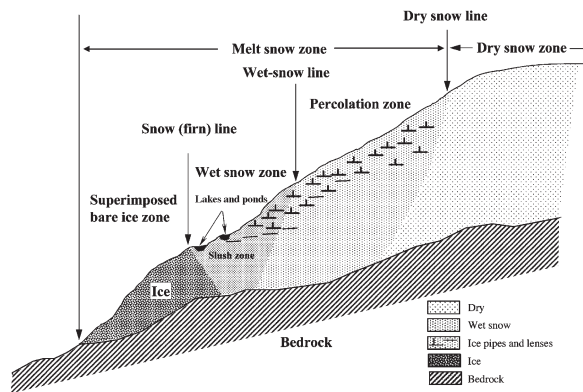


Fig. 3. Schematic representation of different snow zones.

snow pack is dominated by volume scattering from below the snow surface. Surface scattering is insignificant because the snow density is low. Due to the high penetration depth (about 20 m) and predominant volume scattering, the dry snow zone is characterized by low backscatter, and thus generally appears very dark in radar imagery [5], [6], [9]–[11]. An exception to this behavior occurs in East Antarctica. There, snow accumulation is very low, and so slowly growing grains and depth hoar remain near the surface. The result is a marked contrast in brightness between the dry snow zones of East and West Antarctica. Based on *a priori* information and the passive microwave data that we discuss later, we classify the interior East Antarctic region as a dry snow zone, even though this region has a relatively high radar backscatter.

In the snow pack of the percolation zone, occasional or frequent surface melting occurs during summers. Surface meltwater percolates downward, occasionally spreading out into layers. The percolation zone is characterized by large grain sizes and numerous subsurface ice pipes and lenses caused by melt–freeze cycles. The ice pipes and lenses have dimensions larger than or comparable to the wavelength of the SAR and profoundly affect radar backscatter. In the frozen state, the massive subsurface ice layers with large pipes and lenses strongly scatter the radar signal and make the percolation zone appear exceptional bright in radar imagery [9]–[11].

In the wet snow zone, surface melting is intensive and vigorous. The upper snow pack is damp throughout the summer season. At the lower elevations of the wet snow zone, the seasonal presence of free water may produce ponds and lakes in topographical depressions or a slush area. There is strong seasonal dependence in radar backscatter associated with the melt occurrence. During summers, the penetration depth of the radar signal is dramatically reduced to the uppermost 3–4 cm due to the presence of high liquid-water content in the snow pack. The increased absorption of wet snow strongly decreases the strength of backscatter intensity. Therefore, the damp snow corresponds to the darkest tone in radar imagery [5], [9], [10]. During winters, the frozen wet snow zone is characterized by denser and more compacted firn than in the percolation zone. Ice pipes and lenses are less effective backscatters, because of the reduced transmission of the radar signal into the higher-density firn. The wet snow zone is of intermediate brightness in the winter radar imagery due to reduced backscattering [5], [9]–[11].

In the superimposed bare ice zone, snow and firn cover has ablated away. Due to intensive melting, the ice layers in

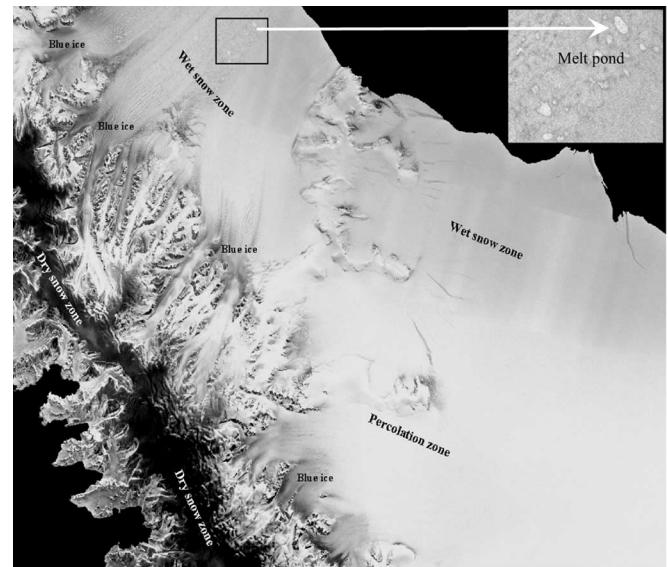


Fig. 4. Radar-backscatter differences between dry snow zones, percolation zones, wet snow zones, and blue ice patches on the Antarctic Peninsula. The frozen melt ponds in the wet snow zone are highlighted in the inset image.

this zone have merged into a continuous ice mass by freezing meltwater. During winters, the bare ice zone exhibits relatively low backscatter compared to that of the firn of the wet snow zone [5], [6].

To sum up, the four snow zones are discernible on radar imagery [11]. The expected brightness-variation pattern on a winter SAR image is: dark for the dry snow zone, exceptional bright for the percolation zone, intermediate bright for the wet snow zone, and intermediate dark for bare ice zone. This pattern has been recognized by field-based radar measurements in [9] and [10] and demonstrated on satellite SAR images in [5] and [11].

C. Radar-Backscatter Signatures of Different Snow Zones in Antarctica

The winter SAR image mosaic has sufficient brightness contrasts for discrimination of different snow zones, and dry snow zones, percolation zones, and wet (soaked) snow zones are present in the Antarctic continent.

As shown in Fig. 4, the strong contrast in radar backscatter exists between dry snow zones and percolation zones. This makes the discrimination between the dry snow zone and the percolation zone relatively easy and reliable. Differences in the radar backscatter between the percolation zone and the wet snow zone are also evident. The frozen melt ponds can be clearly observed in the wet snow zone, as shown in the enlarged inset of Fig. 4. Nevertheless, the overall contrast between the percolation zone and the wet snow zone is not as strong as the contrast between the dry snow zone and the percolation zone. As a consequence, the discrimination of the wet snow zone from the percolation zone is expected to be more difficult and less accurate. The superimposed bare ice zone in Benson's model is absent in Antarctica due to its relatively high latitude. Nevertheless, blue ice patches [15] exposed by sublimation and katabatic wind scouring can be observed in both percolation zones and dry snow zones as isolated islands. In general, the radar-backscatter strength of blue ice patches is lower than wet

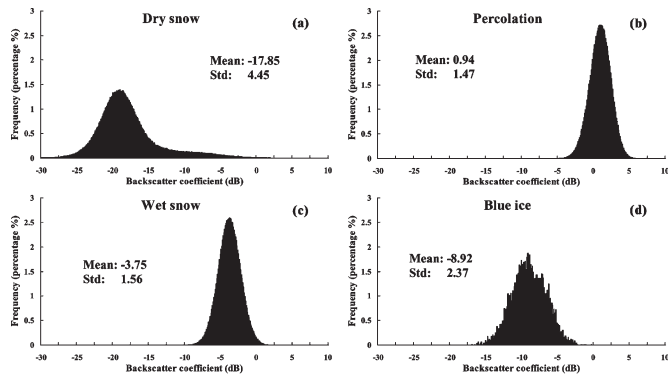


Fig. 5. Histograms of radar backscatter created from the training sites in different snow zones on the Antarctic Peninsula. (a) Dry snow zone. (b) Percolation zone. (c) Wet snow zone. (d) Blue ice patch.

snow zones and higher than dry snow zones in the winter SAR imagery. The spatial extents of blue ice patches are relatively small, and their textures are characterized by ripples, cusps, and stripes caused by katabatic winds and compressive ice flows.

To derive a quantitative signature for each type of snow zone, we identified a number of training sites, respectively, for dry snow zones, percolation zones, wet snow zones, and blue ice patches in different parts of Antarctica. The selection of training sites is based on visual interpretation and also referenced to previous studies [6]. Based on the training data sets, the statistical characteristics of radar backscatter are analyzed for each type of snow zone. Fig. 5 shows the frequency distributions of the radar backscatter in decibels for different snow zones on the Antarctic Peninsula. For the training data sites, the average normalized backscatter coefficient (σ_{na}) and the standard deviation are computed (Fig. 5).

The radar backscattering in mountainous areas is not only influenced by the physical properties of the snow pack but also influenced by the topographical effect. The relief-induced radiometric distortions complicate the recognition of snow zones. The areas with a steep slope facing the radar sensor appear as bright strips in radar images due to the small local incidence angle and the radiometric compression brought about by foreshortening or layover effects. Mountainous areas affected by foreshortening and layover tend to have high radar returns similar to percolation zones. The areas with a steep slope facing away from the SAR sensor have very low radar returns and form radar shadows. The radar shadows appear as dark as dry snow zones in a radar image. In terms of radar-backscattering strength, it is difficult to differentiate radar-foreshortening affected areas from percolation zones and radar shadows from dry snow zones. Nevertheless, both radar-foreshortening and shadow affected areas have a relatively smaller spatial extent and a coarser texture, compared with percolation zones and dry snow zones. It should be noted that foreshortening complications were minimized in the 1997 Antarctic Radarsat SAR image mosaic by using a digital elevation model (DEM) to perform terrain correction and orthorectification. Layover and shadowing effects were minimized by replacing affected pixels with data from different beams and with data from the opposite-looking direction [13], [14]. Residual artifacts remain partly because of the quality of the data used to construct the DEM for mountainous regions.

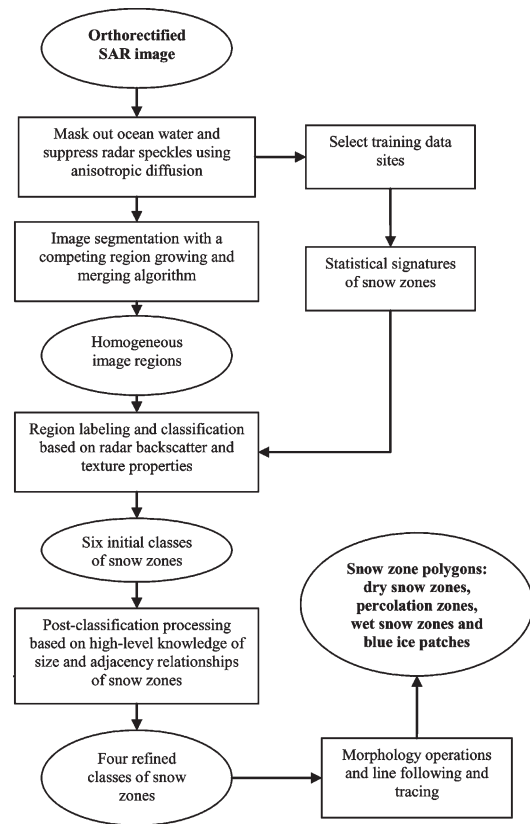


Fig. 6. Data-processing procedure for automated extraction of snow zones from SAR imagery.

D. Automated Algorithms for Snow-Zone Extraction

We designed a chain of image-processing steps to automate the extraction of snow-zone boundaries from the SAR imagery based on the image segmentation. The key processing steps include: image segmentation with a competing region growing and merging algorithm; region classification based on the backscattering and texture properties; and postclassification correction based on higher level knowledge about size and adjacency relationships between snow zones. For the sake of clarity, a flow chart is given in Fig. 6 to outline our algorithms and processing chain. We have implemented the algorithms using the C++ programming language. A working example is shown in Fig. 7 to demonstrate the major processing steps.

First, the SAR image is clipped by the Antarctic coastline [14] to mask out the ocean water portion. Then, we utilize an anisotropic diffusion algorithm [16] to filter and suppress radar speckle [Fig. 7(b)]. Next, the SAR imagery is down sampled from 25- to 100-m pixel size in order to reduce data volume and subsequent computation.

1) *Image Segmentation With a Competing Region Growing and Merging Algorithm*: We developed a competing region growing and merging algorithm to segment the filtered SAR image into a set of relatively homogeneous regions [Fig. 7(c)]. The objective of the segmentation is to partition the entire image R under processing into n regions $\{R_i : i = 1, 2, \dots, n\}$ so that

$$\bigcup_{i=1}^n R_i = R, \quad (R_i \text{ is a connected region, } i = 1, 2, \dots, n) \quad (1)$$

$$R_i \cap R_j = \phi, \quad \text{if } i \neq j \quad (\phi \text{ is the null set}). \quad (2)$$

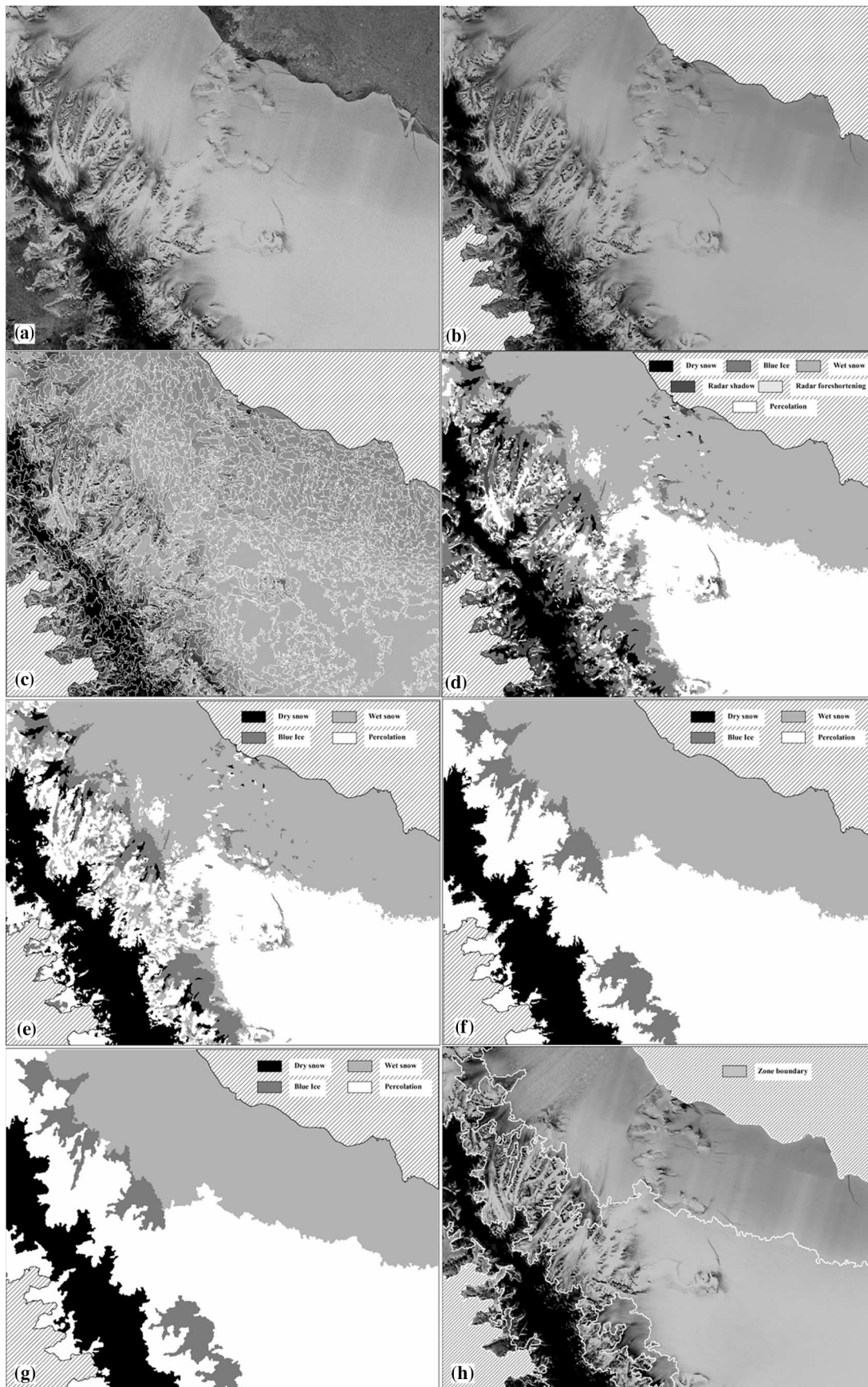


Fig. 7. Classification and postclassification steps for extracting snow zones. (a) Original SAR image. (b) After filtering and clipping. (c) Segmented image. (d) Initially classified image. (e) Postclassification correction after applying rule 1. (f) Postclassification correction after applying rules 2–5. (g) After mathematical morphology operations. (h) Final snow-zone boundaries.

Condition (1) requires that the segmentation must be complete, and condition (2) indicates that the regions must be disjoint and not overlap each other. Our competing region growing procedure groups individual pixels into image regions. It starts with a set of regularly distributed seed points. The spacing between these seed points is adjustable. In our analysis, seed points are deployed at ten-pixel intervals both in row and column directions. These seed points can be considered as one-pixel regions R_i ($i = 1, 2, \dots, n$). We grow the territory of these regions by appending their neighbor pixels according to a competition rule. For each one-pixel region, we examine the radar brightness differences between the seed point and its surrounding neighbors. The minimum difference between the seed point and its neighbors is recorded. We first grow the one-pixel region that has the smallest radar brightness difference from its neighbors. After a region is expanded, the radar brightness differences between the edge pixels of the region and the neighbors of the edge pixels are calculated, and the minimum difference is recorded for the region. For each region, we keep track of the minimum radar brightness difference (d_i) between its edge pixels and their neighboring pixels during the competing growing process

$$d_i = \min_k \left\{ \min_l \{ |E_k - N_k^l| \} \right\}, \quad k = 1, 2, \dots, m \quad (3)$$

where E_k is the radar brightness value of the k th edge pixel of region i , N_k^l is the radar brightness value of the l th neighbor of the edge pixel k , and m is the number of edge pixels of region i . If the region i is expanded, its d_i value is updated. Among all regions R_i ($i = 1, 2, \dots, n$), we select the region R_p for next round of expansion, if $d_p \leq d_i$ ($i = 1, 2, \dots, p - 1, p + 1, \dots, n$). Repeat the above competing growing process until all candidate neighbor pixels have been appended into the image regions.

Since the selection of spatial spacing of seed points is quite arbitrary, the above growing process may create too many regions. In the competition process, some seed pixels may not get a chance to germinate and develop, resulting in some small regions. To improve the segmentation result, a region merging step follows the competing growing process. For two adjacent regions R_i and R_j , if the difference of their mean radar brightness values (M_i and M_j) are smaller than an appropriately selected threshold value T , namely, if $|M_i - M_j| < T$, then regions R_i and R_j are merged into a new region. Since the threshold value T is application dependent, it is coded as an adjustable parameter in our computer program. Based on the knowledge of brightness-value ranges of different snow zones and through visual experiment, the threshold T in our analysis is set to six. This value creates small homogeneous regions whose boundaries follow natural margins of snow-zone patches. The merging order and sequence is determined again by a competing rule. The two adjacent regions that have the smallest difference between their mean radar brightness values are merged first. After two adjacent regions are merged, the mean radar brightness value is computed for the newly merged region. Then, we search all regions (including the newly merged region) and identify the two adjacent regions that have the smallest mean brightness difference for next round of merging. We repeat this competing merging process until there are no adjacent

regions whose mean brightness-value difference is less than the threshold T . A region adjacency graph (RAG) data structure [17] is utilized to realize this competing merging scheme.

The competing region growing and merging algorithm grows and merges regions in a least cost (minimum-difference) direction. Therefore, it ensures that the boundaries and shapes of the resulting regions closely follow the natural margins of various snow zones [Fig. 7(c)]. Our experiments show that this competing region growing and merging algorithm overcomes the segmentation biases and artifacts that often come with conventional segmentation methods like merge, split, and merge-and-split algorithms [18], which use an arbitrary or fixed growing and merging order.

2) *Region Classification Based on Radar Backscatter and Texture Properties*: The image regions derived from the segmentation process are subsequently classified into six classes: dry snow zones, percolation zones, wet snow zones, blue ice patches, radar-shadow affected areas, and radar-foreshortening affected areas [Fig. 7(d)].

In terms of radar-backscattering property, considerable classification ambiguity exists between dry snow zones and radar shadows, between percolation zones and radar-foreshortening affected areas, and between blue ice patches and dry snow zones or wet snow zones. To increase the separability between these features, an image texture measure is introduced in the classification. The texture measure used in our analysis is the contrast index C based on the gray-level co-occurrence matrix (GLCM) computed from a 7×7 window [19], [20]

$$C = \sum_{i=0}^{N-1} \sum_{j=0}^{N-1} |i - j| P(i, j) \quad (4)$$

where N is the number of gray levels (brightness) within the window; i, j are different gray levels (radar brightness values); and $P(i, j)$ represents the relative frequency (the joint probability) that a pair of co-occurring pixels with brightness values i and j appears in the window in separation of one pixel in $0^\circ, 45^\circ, 90^\circ$, and 135° directions. The contrast index C is relatively high for radar-foreshortening and radar-shadow affected areas, medium for blue ice patches, and relatively low for percolation zones, wet snow zones, and dry snow zones.

The classification is based on two feature variables: the mean radar brightness value and the median value of contrast index C for every image region. A maximum-likelihood supervised classification method [18] is used to classify image regions into six classes, in which the statistical signature of each class is derived from the training sites discussed in the preceding section.

3) *Postclassification Processing With Higher Level of Knowledge of Snow Zones*: In order to correct misclassifications and combine radar-shadow and radar-foreshortening affected areas into snow zones, we sequentially apply several postclassification processing steps to the initially classified image. These postclassification operations are designed based on heuristic higher level knowledge about the size of and adjacency relationships between different snow zones. The true snow zones, especially dry snow zones and percolation zones, are spatially extensive. In contrast, radar-foreshortening affected areas, radar-shadow affected areas, and blue ice patches often appear as small broken regions. According to the general snow-zone model, the dry snow zone is spatially separated from

the wet snow zone by the percolation zone. In other words, the spatial adjacency between a dry snow zone and a wet snow zone indicates a misclassification. In Antarctica, a percolation zone is always accompanied by and adjacent to a dry snow zone. A percolation zone without a neighboring dry snow zone also indicates a potential classification error. Based on the above knowledge and facts, we formulate the following postclassification-operation rules.

- 1) If a radar-foreshortening affected area or radar-shadow affected area is adjacent to a dry snow zone, it will be merged into the dry snow zone. Otherwise, it will be merged into the snow zone with which it shares the longest boundary.
- 2) If a wet snow zone is adjacent to a dry snow zone, it will be merged into the dry snow zone. If a wet snow zone is contained in a percolation zone, it will be merged into the percolation zone.
- 3) If a small dry snow zone is contained in a blue ice patch, the small dry snow zone will be merged into the blue ice patch.
- 4) If a small percolation zone is contained in a dry snow zone, it will be merged into the dry snow zone.
- 5) A snow zone of any type with an areal size smaller than a user-specified minimum mapping unit (10 km^2 in our case, much smaller than the pixel size of SSM/I data) will be merged into the adjacent snow zone with which it shares the longest boundary.

The initially classified image has numerous disjoint zones of six classes. Each zone is comprised of spatially connected pixels of the same class. To support the postclassification operations, we calculate and keep track of the areal size and the boundary lengths of each individual zone shared with other adjacent zones through a RAG data structure [17]. By applying rule 1), the mountainous areas affected by radar foreshortening or radar shadow are fused into either dry snow zones or percolation zones [Fig. 7(e)]. By applying rules 2)–5), some misclassified dry snow zones and wet snow zones are corrected and small holes caused by radar speckle and radiometric distortions are also removed. After postclassification operations, we have reduced the classification from six classes to four classes, namely, dry snow zones, percolation zones, wet snow zones, and blue ice patches. These postprocessing steps effectively improve the classification result and provide large continuous snow zones [Fig. 7(f)].

Next, the mathematical morphology operations, consisting of dilation and erosion [17], are applied to smooth and generalize the boundaries of snow zones. The morphological operations close small gaps and “inlets” and remove narrow “peninsulas” in the originally jagged boundaries, and hence give rise to an enhanced cartographical representation of snow-zone boundaries [Fig. 7(g)]. A robust boundary-following algorithm [16] is then used to trace the border pixels of snow zones into boundary polygons. We examined the numerically derived snow-zone boundaries in the ArcGIS environment with reference to original source satellite images. Our visual assessments indicate that algorithm-derived snow-zone boundaries faithfully follow the natural margins of snow zones and closely match our visual interpretation [Fig. 7(h)].

Compared with conventional pixel-by-pixel classification methods, our segmentation-based classification has multiple

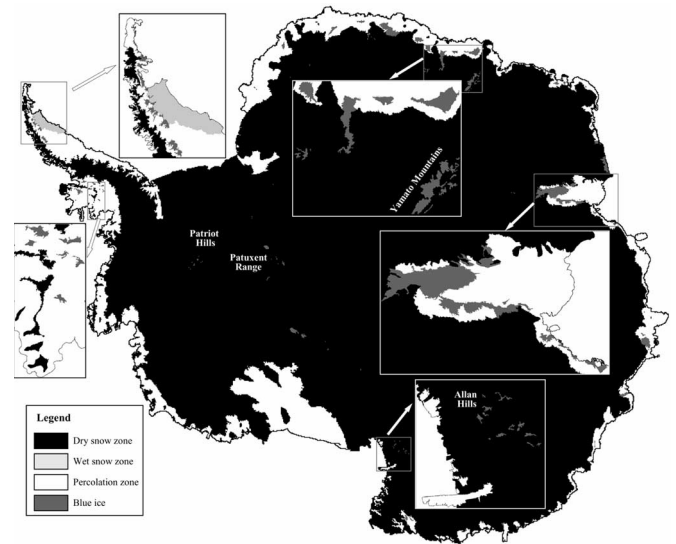


Fig. 8. Dry snow zones, percolation zones, wet snow zones, and blue ice patches in Antarctica derived from 1997 Radarsat SAR image mosaic.

advantages. Owing to the image segmentation, our method preserves the natural edges of the snow zones and avoids the “clutter” classification pattern that commonly goes with pixel-by-pixel classification methods. Due to incorporation of higher level knowledge about geometric properties of and topological adjacency relationships between different snow zones, our method provides a reliable and accurate delineation of various snow zones.

E. Dry Snow Zones, Percolation Zones, Wet Snow Zones, and Blue Ice Patches From SAR Imagery

By applying the above sequence of image-processing algorithms and parameter settings, the snow-zone boundaries are numerically derived for the entire Antarctica with minimal human intervention and editing effort. As shown in Fig. 8, the whole sequence of snow zones in Benson’s model, except for the superimposed bare ice zone, occurs in the Antarctic continent. The interior of the ice sheet and the central plateau of the mountain chain on the Antarctic Peninsula are occupied by dry snow zones. Isolated small dry snow zones are also observed in the top parts of ice rises and islands in the Antarctic coast due to higher elevations (see inset maps of Fig. 8). Most of the Ronne–Filchner ice shelf and the southern and eastern parts of the Ross ice shelf are located in the dry snow zone due to their high latitudes. Overall, the dry snow zones dominate the Antarctic continent, accounting for 89.84% of the total area.

Extensive percolation zones are detected on the ice shelves with relatively low latitude, including the Larsen ice shelf, George IV ice shelf, Amery ice shelf, West ice shelf, ice shelves along Queen Maud Land and Marie Byrd Land, and the western part of the Ross ice shelf. The percolation zones on the grounded ice sheet are confined to a narrow band of varying width near the coast (Fig. 8). The percolation zone indicates the extent of snow surface that are at least occasionally affected by melt events.

In Antarctica, the extent of the wet snow zone is spatially insignificant. It is only distributed on the northern part of the Antarctic Peninsula. The Antarctic Peninsula has a relatively

well-developed snow-zone sequence, particularly on the eastern side of the peninsula. The progressive transitions from the wet snow zone to the percolation and then to the dry snow zone is manifestly visible, when moving from the coast to the central mountain plateau.

The detected blue ice patches are distributed in both percolation zones and dry snow zones where the surface slope is relatively steep. Solid bluish ice fields are renowned as meteorite collection sites and ideal inland runway sites [15]. As shown in Fig. 8, small blue ice patches are distributed in the percolation zones on the Antarctic Peninsula, in the Amery ice shelf region, and in the Queen Maud Land region. The expanses of blue ice fields are also detected in dry snow zones in the Transantarctic Mountains near Allan Hills and Patuxent Range, in the Ellsworth Mountains near Patriot Hills, and in the Yamato (Queen Fabiola) Mountains and Sør Rondane Mountains in Queen Maud Land (Fig. 8). The blue ice areas arise largely because of the upwelling of deep glacial ice on the flanks of the mountains and nunataks, surface snow being blown away by gusty Katabatic winds, and the firn sublimating away to the atmosphere. The blue ice areas are not located at a lower elevation as a continuous zone surrounding the wet snow zone. In terms of the location, formation, spatial extent, and continuity, the isolated blue ice patches cannot be regarded as the superimposed bare ice zone in Benson's model.

III. DELINEATION OF MELT SNOW ZONES USING SSM/I DATA

A. Physical Basis and Algorithm for Melt Detection With Passive Microwave Data

A passive microwave sensor detects the naturally emitted microwave energy from the snow pack within its field of view. The passive microwave data are brightness temperatures calibrated from the recorded microwave energy. The physical mechanism for melt-detection algorithms is that the microwave emissivity and brightness temperature (T_b) of a snow pack increases dramatically in response to the introduction of even a small amount of liquid-water content during the snow-melt season [21], [22]. A sharp and abrupt transition in the microwave brightness temperature (T_b) is the distinct signature of melt occurrence, which is detectable by microwave sensors at frequencies in excess of 10 GHz [22]. The analysis of time-series passive microwave data enables the discrimination of the melt snow zone from the dry snow zone. Due to very coarse spatial resolution and relatively smooth transition of brightness temperature, satellite passive microwave data are not adequate for differentiating the percolation zone and the wet snow zone. Temporal analysis of passive microwave data is intended to demarcate the snow surface area into the melt snow zone and dry snow zone and to examine the spatial variation of melt duration within the melt snow zone.

We used the daily passive microwave SSM/I data in our snow-melt analysis. The SSM/I sensors have seven different channels. Our experiments showed that although all channels show similar responses to melt events, the 19-GHz (1.55-cm wavelength) horizontally polarized channel exhibits the strongest melt-induced edges on the T_b time series, and hence was employed in our analysis [12]. The resampled pixel size for this channel is 25 km.

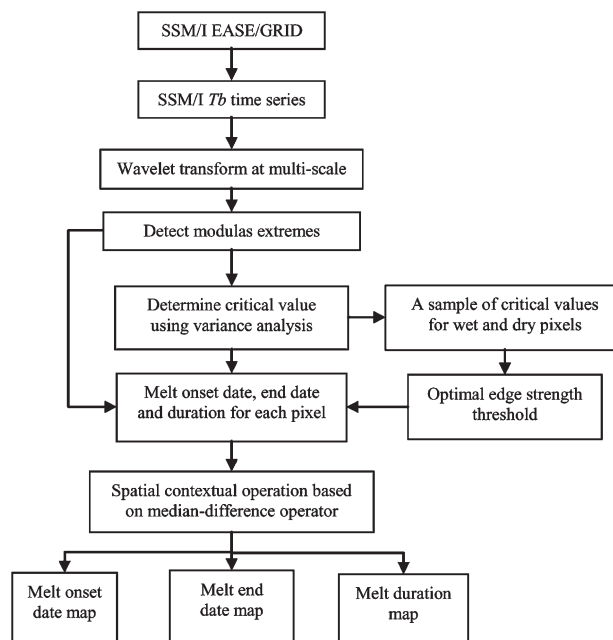


Fig. 9. Data flow chart for deriving the dry snow zone and snow-melt zone with SSM/I data.

We developed a multiscale wavelet-transform-based method for deriving snow-melt onset date, melt end date, melt duration, and melt extent. To obtain the precise timing of melt and freeze occurrences, our method explicitly searches and tracks strong edges on daily brightness-temperature curves induced by melt and refreeze events across scales. The computational procedure is summarized in Fig. 9, and a detailed description of the algorithms can be found in [12].

B. Melt Extent and Duration Derived From SSM/I Data

In order to compare and correlate the snow zones detected from the 1997 winter SAR imagery, we processed the satellite passive microwave SSM/I data from July 1, 1991 to June 30, 1997 collected by the DMSP F8, F11, and F13 satellites. The melt onset date, melt end date, and melt duration are computed sequentially for every data pixel. The pixel-by-pixel computation produces three grids each year during 1991–1997: melt onset-date grid, melt end-date grid, and melt duration grid.

The melt onset-date map [Fig. 10(a)] shows the melt-wave progression as seasonal air temperature increase for the 1996/1997 austral summer season. The melt end-date map [Fig. 10(b)] shows the spatial pattern of melt-wave retreat. The annual variations of the melt snow extent and duration during 1991–1997 are shown in Fig. 11.

IV. COMPARISONS AND DISCUSSIONS

Analysis results derived from active microwave SAR imagery and passive microwave SSM/I data indicate that Antarctic ice surface melting is sparse and concentrated in the periphery of the Antarctic continent. However, the spatial coverage of the melt snow zones derived from the 1997 winter SAR image mosaic is significantly different from that detected from the SSM/I daily brightness-temperature data during the 1996/1997 austral summer [Fig. 12(a)]. The matching rate between the

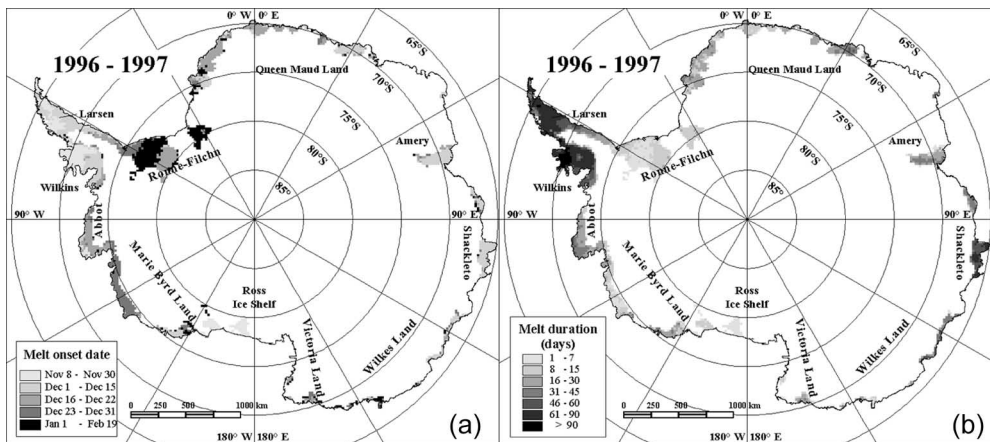


Fig. 10. Snow-melt pattern for the austral summer during 1996–1997. (a) Melt onset date. (b) Melt end date.

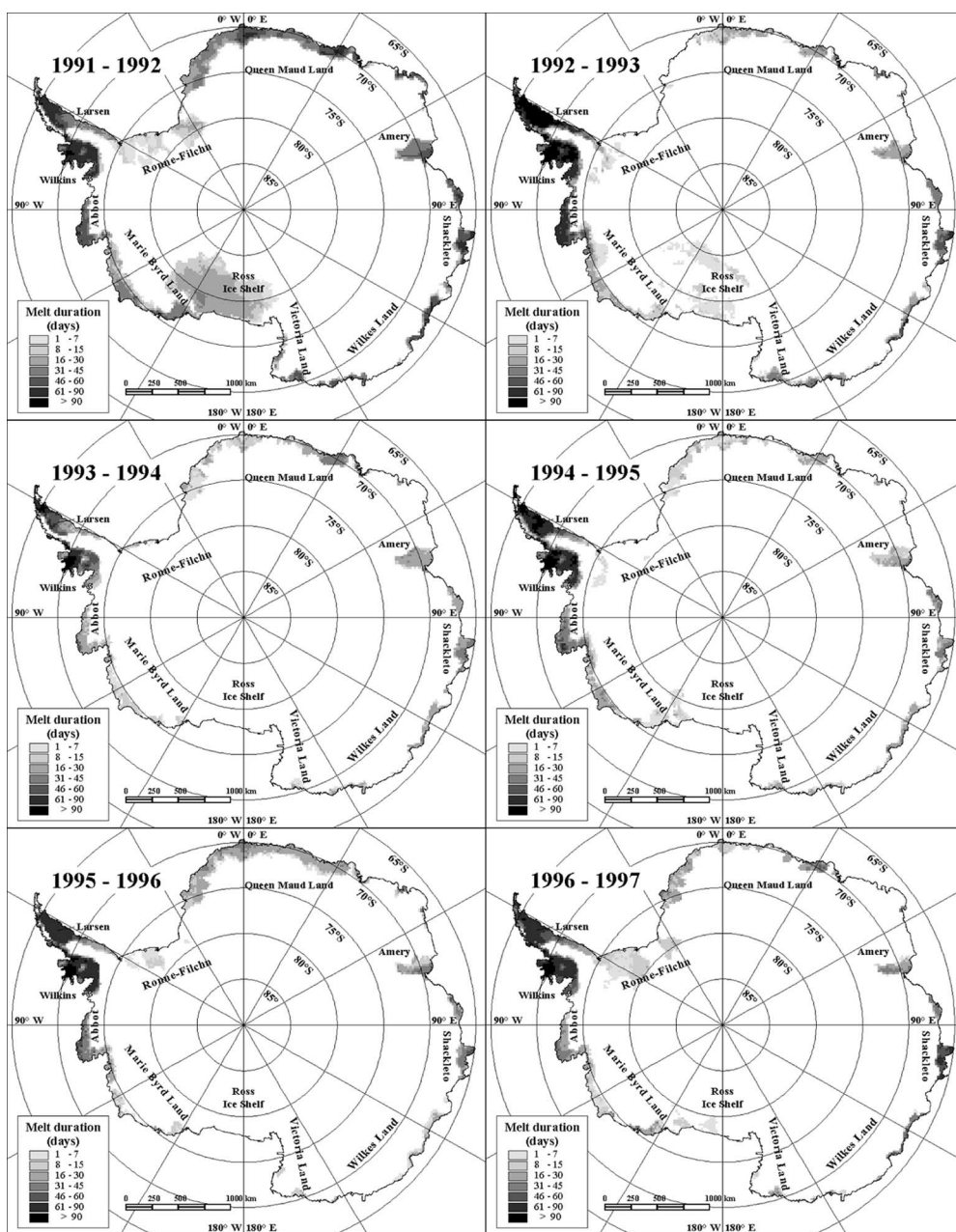


Fig. 11. Annual variability in snow-melt extent and duration (cumulative melt days) during 1991–1997 detected with the SSM/I data.

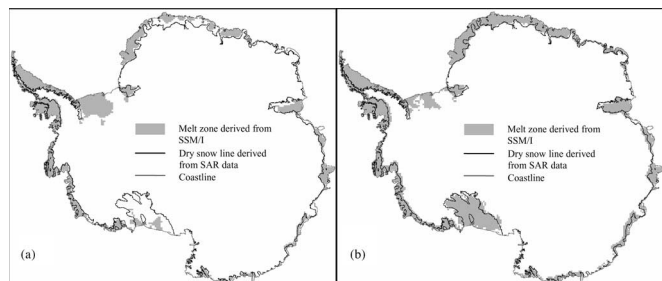


Fig. 12. Snow-zone boundaries derived from the 1997 SAR image mosaic compared with snow-melt extents derived from passive microwave data. (a) The shaded area is the snow-melt extent during the 1996/1997 austral summer. (b) The shaded area is comprised of pixels whose average annual melt duration in the past six austral summers from 1991 to 1997 is longer than three days.

SAR-derived melt zone extent and the passive microwave-derived melt extent for the 1996/1997 summer is only 61%. The discrepancies suggest that the melt snow zone from SAR imagery does not represent the melt extent for the year when the SAR imagery was acquired. Notably, no surface melting was observed from the passive SSM/I data in many small ice shelves along the coast of Queen Maud Land. However, the percolation zones were detected in these regions from the 1997 winter SAR imagery. An extensive percolation zone is delineated from the SAR imagery on the Ross ice shelf, where only brief melting for two small areas was detected by the passive microwave sensor. In addition, the effect of the short-lived melting in the rim of the Ronne–Filchner ice shelf in the 1996/1997 austral summer detected from passive microwave SSM/I data does not show up on the 1997 winter SAR imagery. This is likely because the melting is not intensive enough to develop the ice pipes and ice lenses, or because new snowfall after the summer precluded the melting effect from being detected by the SAR sensor. It is known that the Ronne–Filchner ice shelf has a much higher snow-accumulation rate than the Ross ice shelf [23].

As shown in Fig. 12(b), the averaged snow-melt extent during 1991–1997 derived from the passive microwave SSM/I data has a much better correspondence with that derived from the 1997 winter SAR image mosaic. The shaded area in Fig. 12(b) represents the cumulative melt area with averaged annual melt duration of at least three days during the austral summers from 1991 to 1997. The matching rate between the snow-melt extent derived from the 1997 SAR image and the averaged snow-melt extent during 1991–1997 detected by the passive microwave data is 93%. The greatly improved match suggests that the snow-melt zone derived from SAR imagery represents a composite signal of intermittent melt events summed over many years. In areas with low accumulation (less than the radar penetration depth) in intermittent melt years, the radar-backscatter signal may still be strong even though the last melt event may have occurred years ago. In the case of the Ross ice shelf, a short period but spatially extensive melting was detected during the 1991/1992 austral summer, and no substantial surface melting was detected afterwards until 1997 (Fig. 11). The melting effect was still detected by the SAR sensor after six years, and hence, an extensive percolation zone was delineated. This is attributable to the extremely low snow accumulation on the Ross ice shelf [23].

The above observation can be explained by the fact that active and passive microwave sensors rely on different physical

mechanisms to detect and map snow zones. Passive microwave sensors depend on the daily variations in snow emissivity and brightness temperature, which are induced by the changes in the liquid-water content of the snow pack. Therefore, melt snow zones detected from passive microwave data represent the melt extent at the time of data acquisition. In contrast, active microwave SAR sensors rely more on spatial differences in radar-backscatter strength, which are affected by relatively long-term and cumulative variations of the grain size, density, subsurface ice layers, stratigraphy, and surface roughness of the snow pack. Consequently, melt snow zones detected from SAR imagery, including percolation zones and wet snow zones, represent the cumulative melt extent over a number of years prior to the image acquisition date.

Since active microwave SAR imagery has a high spatial resolution (25 m), relatively small snow zones like dry snow zones on the tops of ice rises and narrow percolation zones on the grounded ice sheet have been detected and mapped (see inset maps of Fig. 8). Even though the SSM/I data were resampled into $25 \text{ km} \times 25 \text{ km}$ pixels for the 19-GHz channel, the natural resolution (the effective field of view) is 70 km along track and 45 km cross track. The brightness temperature of each data pixel represents the average snow condition over approximately 3150 km^2 . Consequently, individual snow zones smaller than this size cannot be reliably detected. Many small-size dry and percolation zones that are discernable on the SAR image mosaic were missed by the SSM/I data.

The comparative advantage of the passive microwave sensor lies in its high temporal resolution. The daily observations of brightness temperatures enable the determination of the melt onset date, melt end date, and the length of melt duration. The timing of melt occurrence cannot be derived from a one-time snapshot of active microwave radar imagery. The spatial progression of melting, spatial variation in melt duration, and interannual variability in the extent of melt snow zones can be detected and monitored with the passive microwave data (Fig. 11).

The wet snow zone delineated from the 1997 winter SAR image mosaic represents the areas where the most intensive surface melting occurred in the Antarctic continent. By correlating the surface-melt information derived from the passive microwave data, we determined that the average annual melt duration in the wet snow zone is 80 days (with a standard deviation of 12 days) during 1991–1997, 23 days longer than the adjacent percolation zone on the Antarctic Peninsula. The annual melt duration of 80 days may be regarded as a threshold to recognize the wet snow zone with the passive microwave data. The differentiation between the percolation zone and the wet snow zone are valuable for investigating the mass balance and stability of the glacial system. In the percolation zone, redistribution of melt water is limited horizontally and vertically near the surface, and melt processes yield no mass loss to the ice sheet and ice shelves. In contrast, melt water produced in the wet snow zone can be potentially discharged from the ice sheet to the sea, resulting in a net loss of mass. In the Antarctic continent, the detected wet snow zone was located in the northern part of the Larsen ice shelf on the Antarctic Peninsula. Most of this wet snow zone catastrophically disintegrated in 2002 [24]. This suggests that the wet snow zone is the most vulnerable part in the Antarctic glacial system. Scambos *et al.* [25] suggested

that mysterious break-ups of this wet snow zone were correlated with intensive melting and the ponded melt water.

V. CONCLUSION

In this paper, we presented numerical algorithms for delineating snow zones with active microwave SAR image data. A segmentation-based classification method is developed to extract snow zones from the SAR imagery. The innovative utilization of the higher level knowledge about the size and adjacency properties of snow zones in the postclassification processing greatly reduces classification errors and minimizes human editing effort. The algorithm used with the passive microwave data is based on multiscale wavelet transform of daily brightness temperatures. The successful delineation of snow zones over the entire Antarctic continent demonstrates that our algorithms are effective and efficient.

Our analysis shows that surface melting in the Antarctic continent is relatively sparse and short lived. While the whole sequence of snow zones has been identified for the Greenland ice sheet [1], [11], the superimposed bare ice zone is absent in Antarctica due to its high latitude and less-intensive surface melting. The dry snow zone dominates the Antarctic continent, and melt snow zones account for only 10.2% of its snow surface.

We demonstrate that both active and passive satellite microwave sensors are useful for the discrimination of the melt snow zone from the dry snow zone. The active microwave SAR image data have advantages in spatial resolution (25 m), but provide less-frequent coverage. In contrast, the passive microwave satellite data span more than 25 years and provide temporally frequent observations on a daily basis, but the spatial resolution is coarse (25 km). Passive microwave data can only provide a coarse discrimination of melt snow zones from dry snow zones. The active microwave SAR imagery supports further differentiation between the percolation zone and the wet snow zone within a melt snow zone. The blue ice patches and fields can be also reliably delimited from the SAR imagery. Passive microwave data offer a strong capability in determining the timing (onset date and end date) and duration of melt occurrences, which cannot be derived from active microwave radar imagery. Due to the complementary nature, the combination of active and passive microwave data provides a better view of the properties of the snow pack in different snow zones.

It should be emphasized that the melt snow zones derived from active and passive microwave data need to be interpreted differently. Our analysis suggests that the melt snow zone extracted from active SAR imagery does not necessarily coincide with the snow-melt extent for the year when the satellite SAR imagery was acquired. Instead, it represents the snow-melt extent integrated over many years prior to the SAR image acquisition. In contrast, melt snow zones delineated from the passive microwave data at a much coarser spatial resolution indicate snow-melt extent directly corresponding to the acquisition date of the passive microwave data.

ACKNOWLEDGMENT

The authors would like to thank the National Snow and Ice Data Center (Boulder, CO) for providing the SSM/I

EASE-Grid brightness-temperature data for this research project.

REFERENCES

- [1] C. S. Benson, "Stratigraphic studies in the snow and firn of the Greenland ice sheet," U.S. Army Corps Eng., Hannover, NH, SIPRE Res. Rep. 70, 1962.
- [2] W. S. B. Paterson, *The Physics of Glaciers*, 3rd ed. New York: Pergamon, 1994.
- [3] K. Steffen, "Surface energy exchange at the equilibrium line on the Greenland ice sheet during onset of melt," *Ann. Glaciol.*, vol. 21, no. 1, pp. 13–18, 1995.
- [4] R. S. J. Williams, D. K. Hall, and C. S. Benson, "Analysis of glacier facies using satellite techniques," *J. Glaciol.*, vol. 37, no. 125, pp. 120–128, 1991.
- [5] K. C. Partington, "Discrimination of glacier facies using multi-temporal SAR data," *J. Glaciol.*, vol. 44, no. 146, pp. 42–53, 1998.
- [6] F. Rau and M. Braun, "The regional distribution of the dry-snow zone on the Antarctic Peninsula north of 70 °S," *Ann. Glaciol.*, vol. 34, no. 1, pp. 95–100, Jan. 2002.
- [7] W. Abdalati and K. Steffen, "Greenland ice sheet melt extent: 1979–1999," *J. Geophys. Res.*, vol. 106, no. D24, pp. 33 983–33 989, 2001.
- [8] M. Joshi, C. J. Merry, K. C. Jezek, and J. F. Bolzan, "An edge detection technique to estimate melt duration, season and melt extent on the Greenland ice sheet using passive microwave data," *Geophys. Res. Lett.*, vol. 28, no. 18, pp. 3497–3500, 2001.
- [9] K. C. Jezek, M. R. Drinkwater, J. P. Crawford, R. Bindshadler, and R. Kwok, "Analysis of synthetic aperture radar data collected over south-western Greenland ice sheet," *J. Glaciol.*, vol. 39, no. 131, pp. 119–132, 1993.
- [10] K. C. Jezek, P. Gogineni, and M. Shanableh, "Radar measurements of melt zones on the Greenland ice sheet," *Geophys. Res. Lett.*, vol. 21, no. 1, pp. 33–36, 1994.
- [11] M. A. Fahnestock, R. Bindshadler, R. Kwok, and K. C. Jezek, "Greenland ice sheet surface properties and ice dynamics from ERS-1 SAR imagery," *Science*, vol. 262, no. 5139, pp. 1530–1534, 1993.
- [12] H. Liu, L. Wang, and K. Jezek, "Wavelet-transform based edge detection approach to derivation of snowmelt onset, end and duration from satellite passive microwave measurements," *Int. J. Remote Sens.*, vol. 26, no. 21, pp. 4639–4660, 2005.
- [13] K. C. Jezek, "Radarsat-1 Antarctic mapping project: Change detection and surface velocity campaign," *Ann. Glaciol.*, vol. 34, no. 1, pp. 263–268, Jan. 2002.
- [14] H. Liu and K. C. Jezek, "A complete high-resolution coastline of Antarctica extracted from orthorectified Radarsat SAR imagery," *Photogramm. Eng. Remote Sens.*, vol. 70, no. 5, pp. 605–616, 2004.
- [15] R. S. Williams, T. K. Meunier, and J. G. Ferrigno, "Blue ice, meteorites, and satellite imagery in Antarctica," *Polar Rec.*, vol. 22, no. 134, pp. 493–496, 1983.
- [16] H. Liu and K. Jezek, "Automated extraction of coastline from a satellite imagery by integrating Canny edge detection and locally adaptive thresholding methods," *Int. J. Remote Sens.*, vol. 25, no. 5, pp. 937–958, 2004.
- [17] M. Sonka, V. Hlavac, and R. Boyle, *Image Processing, Analysis and Machine Vision*, 2nd ed. Pacific Grove, CA: Brooks/Cole, 1999.
- [18] R. C. Gonzalez and R. Wintz, *Digital Image Processing*. Reading, MA: Addison-Wesley, 1987.
- [19] R. M. Haralick, K. Shanmugam, and I. Dinstein, "Textual features for image classification," *IEEE Trans. Syst., Man, Cybern.*, vol. SMC-3, no. 6, pp. 610–621, Nov. 1973.
- [20] J. R. Parker, *Algorithms for Image Processing and Computer Vision*. New York: Wiley, 1997.
- [21] H. J. Zwally and P. Gloersen, "Passive microwave images of polar regions and research applications," *Polar Rec.*, vol. 18, no. 116, pp. 431–450, 1977.
- [22] F. T. Ulaby, R. K. Moore, and A. Fung, *Microwave Remote Sensing: Active and Passive*, vol. III. Norwood, MA: Artech House, 1986.
- [23] M. B. Giovinetto and H. J. Zwally, "Spatial distribution of net surface accumulation on Antarctic ice sheet," *Ann. Glaciol.*, vol. 31, no. 1, pp. 171–178, Jan. 2000.
- [24] D. R. MacAyeal, T. A. Scambos, C. L. Hulbe, and M. A. Fahnestock, "Catastrophic ice-shelf break-up by an ice-shelf-fragment-capsizing mechanism," *J. Glaciol.*, vol. 49, no. 164, pp. 22–36, 2003.
- [25] T. A. Scambos, C. Hulbe, M. Fahnestock, and J. Bohlander, "The link between climate warming and break-up of ice shelves in the Antarctic Peninsula," *J. Glaciol.*, vol. 46, no. 154, pp. 516–530, 2000.



Hongxing Liu (M'02–A'02–M'04) received the Ph.D. degree in geography from The Ohio State University, Columbus, in 1999.

He is currently an Associate Professor in the Department of Geography, Texas A&M University, College Station. His research interests include remote sensing, geographical information science, hydrological modeling, terrain analysis, coastal mapping, and change studies. His recent research projects have been funded by the National Aeronautics and Space Administration, the National Science Foundation,

and the National Oceanographic and Atmospheric Administration Sea Grant Program.

Dr. Liu has received a number of prestigious awards, including the NASA Group Achievement Award, the Best Paper Award from Computers and Geoscience, and the Distinguished Achievement Award in Teaching from the College of Geoscience at Texas A&M University.



Kenneth C. Jezek (A'92) received the Ph.D. degree in geophysics from the University of Wisconsin, Madison, in 1980.

He was the Director of the Byrd Polar Research Center, The Ohio State University, Columbus, from 1989 to 1999. He is currently a Professor at the Byrd Polar Research Center and in the Department of Geology, The Ohio State University. Now, he leads a research team studying the Earth's polar regions using satellite remote sensing techniques.



Lei Wang was born in Lan Zhou, China, on October 3, 1974. He received the B.S. degree in geography from Beijing University, Beijing, China, in 1997, and the M.S. degree in cartography and geographic information system from the Institute of Remote Sensing Applications of the Chinese Academy of Sciences, Beijing, in 2000. He is currently working toward the Ph.D. degree at Texas A&M University, College Station. His Ph.D. dissertation research has been supported by a National Aeronautics and Space Administration Earth System Science Fellowship.

His research interests include remote sensing, image analysis and processing, geographic information science, and hydrological modeling.